Intrinsic thermal conductivity of ZrC from low to ultrahigh temperatures: A critical revisit

Janak Tiwari and Tianli Feng

Intrinsic thermal conductivity of ZrC from low to ultra-high temperatures: A critical revisit

Janak Tiwari, Tianli Feng*

Department of Mechanical Engineering, University of Utah, Salt Lake City, UT 84112, USA

Corresponding Author:

*tianli.feng@utah.edu

ABSTRACT

Current phonon transport theory based on ground-state calculations has been successful in predicting thermal conductivity at room and medium temperatures but may misrepresent behavior at high temperatures. In this work, we predict the thermal conductivity (κ) of ZrC including electronic and phonon contributions from 300 K to 3500 K, by including high-order phonon scattering, lattice expansion, temperature-dependent (TD) 2nd, 3rd, 4th-order force constants (2FC, 3FC, 4FC), and inter-band phonon conduction by using first principles. For the phonon transport, we find that four-phonon scattering (4ph) significantly reduces the phonon thermal conductivity (κ_{ph}), as much as by ~75% at 3500 K. After including 4ph scattering and all other factors, κ_{ph} shows a ~$T^{-1.5}$ rather than ~T^{-1} dependence. TD 2FC decreases three-phonon scattering (3ph) rates but increases 4ph rates by decreasing and increasing the scattering phase spaces, respectively. For 4ph phase space, the TD 2FC flattens phonon bands, and allows more redistribution 4ph processes (1+2$\rightarrow$3+4) to happen. The combination effect of TD 2FC and TD 4FC reduces 4ph rates of acoustic modes but increases those of optical modes. The TD 3FC and 4FC decrease the phonon scattering cross-section and increase the κ_{ph} significantly (by 52% at 3500 K). The contribution from inter-band (Wigner) phonon conduction is small, even at ultra-high temperatures. For electronic thermal transport, we find that it is sensitive to and can be changed by 20% by the TD lattice constants. The Lorenz number varies from 1.6 to 3.3×10^{-8} W Ω K^{-2} at different temperatures. The theoretical prediction in the literature overpredicts κ_{ph} (e.g., ~28%) and underpredicts the κ_{el} (e.g., ~38%), resulting in an overall underprediction of κ (~26% at 1500 K). The impacts of grain

size and defects are found strong, and no reported experimental data has reached the intrinsic theoretical thermal conductivity of ZrC yet.

Keywords: *Ultra-high temperatures, temperature-dependent force constant, ZrC, first principle prediction*

I. INTRODUCTION

High melting point [1,2], high hardness [3], good thermal conductivity [4,5], excellent chemical stability, good electrical conductivity [5], high strength and stiffness [6,7], and resistance to oxidation even at high temperature [8] makes ZrC a suitable material for various high-temperature engineering applications [9–13] such as rocket nozzles, turbine blades, heat shields, cutting tools, refractory materials, armor materials, etc. Furthermore, ZrC is a common material used in the nuclear industry due to its ability to withstand high temperatures and radiation exposure, making it an ideal choice for fuel elements [14,15]. In addition to these applications, ZrC is also used to make electrodes in batteries and fuel cells [16,17]. To effectively design and optimize these applications, a thorough understanding of the underlying heat transfer mechanism on ZrC is necessary.

The study of heat transfer mechanisms in ZrC has been a topic of great interest. Many experimental thermal conductivity data of ZrC from room temperature up to its melting point (~3700 K) have been reported [4,5,18–23]. However, the measured thermal conductivity data are scattered across the literature. For example, at room temperature, the values vary from as low as 20 W m^{-1} K^{-1} to as high as 40 W m^{-1} K^{-1}, and at 2000 K, they are scattered from 22 to 46 W m^{-1} K^{-1}. ZrC is a semi-metallic material, with the total thermal conductivity (κ) arising from the combined effect of electronic (κ_{el}) and lattice thermal conductivity (κ_{ph}). However, since direct measurement of lattice thermal conductivity is challenging, it is typically derived from the total thermal conductivity by subtracting the electronic contribution by the Wiedemann-Franz law [24,25]. This approach leaves some uncertainty because the Lorenz number (L) is not necessarily $L_0 = 2.44 \times 10^{-8}$ W Ω K^{-2}. Moreover, κ_{ph} is found to be more sensitive to external factors such as defects, grain boundaries, and impurities than κ_{el}, making it further challenging to unveil the intrinsic thermal conductivity directly from the existing experimental data.

2

Different theoretical studies [26–29] based on molecular dynamics (MD) and density functional theory (DFT) have been done to understand the thermal conductivity of ZrC. Crocombette [26] studied the phonon and electronic thermal conductivity of ZrC from 1000 to 3500 K using molecular dynamics (MD). They further found that the impacts of defects are strong. Although they account for the temperature effect and predict thermal conductivity correctly using MD, they did not discuss intrinsic scattering and fundamental thermal transport mechanisms. Zhou, Fahrenholtz, Graham, and Hilmas found that carbon vacancy [27] and Hf additive [28] greatly suppress the phonon thermal conductivity by using first-principles calculations. However, their results are based on the Debye-Callaway model (of which accuracy can be questionable) and ignored the higher order scattering, which is found important at elevated temperatures [30,31]. Moreover, their study is focused only on lattice thermal conductivity. Mellan, Aziz, Xia, Grau-Crespo and Duff [29] predicted the thermal conductivity of ZrC by incorporating both three phonon scatterings (3ph) and four phonon scatterings (4ph), as well as phonon renormalization for the 2nd order force constant. However, their calculations were only based on ground state force constants (GSFC), which may not be accurate for high-temperature calculations as found in Ref [32]. In this work, we predict the thermal conductivity of ZrC by including high-order phonon scattering, lattice expansion, and temperature-dependent force constants (TDFC). We also calculate the off-diagonal (Wigner) thermal conductivity, which is found to be significant for various materials at high temperatures. Additionally, we have analyzed the impact of extrinsic factors such as grain boundary scattering, defect scattering, and impurity scattering on phonon thermal conductivity at different temperatures.

II. METHODOLOGY

ZrC is a semi-metallic material with thermal conductivity (κ) being

$$\kappa = \kappa_{ph} + \kappa_{el} . \tag{1}$$

Based on the Boltzmann transport equation (BTE), the κ_{ph} can be calculated as:

$$\kappa_{ph}^{\alpha\beta} = \sum_{\lambda} c_{\lambda} v_{\lambda}^{\alpha} v_{\lambda}^{\beta} \tau_{\lambda}^{ph} , \tag{2}$$

where $\lambda = (\mathbf{q}, \upsilon)$ denotes the phonon mode with wave vector $\mathbf{q}$ and polarization υ. c_λ is the specific heat per mode, v_λ^α and v_λ^β are phonon group velocities along α and β directions. τ_λ^{ph} is the phonon relaxation time and can be calculated using $\frac{1}{\tau_\lambda^{ph}} = \frac{1}{\tau_\lambda^{ph-ph}} + \frac{1}{\tau_\lambda^{ph-i}} + \frac{1}{\tau_\lambda^{ph-el}}$ where the three terms on the right are phonon-phonon (including 3ph and 4ph), phonon-isotope, and phonon-electron (ph-el) scattering rates, respectively.

Similarly, κ_{el} is calculated based on BTE and Onsager [33] relations as:

$$\sigma_{\alpha\beta} = -\frac{e^2 \, n_s}{V} \sum_{i\mathbf{k}} \frac{df_{i\mathbf{k}}}{d\varepsilon} \, v_{i\mathbf{k}}^\alpha \, v_{i\mathbf{k}}^\beta \tau_{i\mathbf{k}}^{el} \tag{3}$$

$$[\sigma S] = -\frac{e \, n_s}{VT} \sum_{i\mathbf{k}} (\varepsilon_{i\mathbf{k}} - \mu) \frac{df_{i\mathbf{k}}}{d\varepsilon} \, v_{i\mathbf{k}}^\alpha \, v_{i\mathbf{k}}^\beta \tau_{i\mathbf{k}}^{el} \tag{4}$$

$$K_{\alpha\beta} = -\frac{n_s}{VT} \sum_{i\mathbf{k}} (\varepsilon_{i\mathbf{k}} - \mu)^2 \frac{df_{i\mathbf{k}}}{d\varepsilon} \, v_{i\mathbf{k}}^\alpha \, v_{i\mathbf{k}}^\beta \tau_{i\mathbf{k}}^{el} \tag{5}$$

Here, $\sigma_{\alpha\beta}$ and $S_{\alpha\beta}$ denotes the electrical conductivity and Seeback coefficient. $K_{\alpha\beta}$ is used to calculate κ_{el} as $\kappa_{el} = K - S\sigma ST$. e is the elementary charge, $\mathbf{k}$ is the electronic wave vector at band index i, V is the volume of the primitive cell, $f_{i\mathbf{k}}$ is Fermi-Dirac distribution. $\varepsilon_{i\mathbf{k}}$ and μ denotes electron energy and chemical potential respectively. $v_{i\mathbf{k}}$ and $\tau_{i\mathbf{k}}^{el}$ denotes electron velocity and relaxation time and α and β are directional components. The formulation is referred from Refs. [33,34]

Extrinsic scattering rates due to grain boundary $\left(\tau_{gb,\lambda}^{-1} \right)$ and vacancy $\left(\tau_{d,\lambda}^{-1} \right)$ are calculated using the respective formulation shown in Equation (6) and Equation (7) respectively.

$$\tau_{gb,\lambda}^{-1} = \frac{v_{ph,\lambda}}{D_{grain}} \tag{6}$$

$$\tau_{d,\lambda}^{-1} = 9\frac{\pi}{2} f_v \omega_\lambda^2 \cdot \mathrm{pDOS}(\omega) \tag{7}$$

Here, λ represents phonon mode $(\mathbf{q}, j)$ with $\mathbf{q}$ and j labeling the phonon wave vector and dispersion branch, respectively. v_{ph} represents the phonon group velocity at λ, and D_{grain} is the grain size.

Similarly, and f_v represents the concentration of the vacancy. Likewise, ω represents the angular velocities and $\text{pDOS}(\omega)$ represents the partial density of states of a basis atom. The coefficient 9 in Equation (7) accounts for the mass and bond loss associated with the defect vacancy. [35,36] More detail on the extrinsic scattering rates calculation can be found in Ref. [37] and Supplemental Material [38].

Figure 1 shows the computational workflow of the study. The first principles calculations based on DFT are performed by using Vienna Ab initio Simulation Package (VASP) [39,40], using projected augmented wave (PAW) [41] method and Perdew-Burke-Ernzerhof (PBE) [42] functional. ZrC belongs to the Fm3m space group and exhibits a cubic FCC structure. The plane-energy cutoff is 500 eV and the energy and force convergence threshold are 2×10^{-8} eV and 2×10^{-8} eV Å^{-1}, respectively. The relaxed lattice constant is 4.710 Å, which closely resembles the experimental value [2] of 4.694 Å. Harmonic (2nd-order) force constants (HFC or 2FC) are extracted using Phonopy [43]. The anharmonic force constants (AFC), including 3rd (3FC) and 4th order (4FC), are calculated using Thirdorder and Fourthorder packages built inside ShengBTE [44], considering the 4th and 2nd nearest atoms, respectively. In all DFT calculations, supercells of 4×4×4 (128 atoms) are used with a **k**-point grid of 6×6×6. Temperature-dependent 2nd, 3rd, and 4th order force constants are obtained by the TDEP method [45,46] with the input being the energy, forces, and stresses of atoms in randomly a displaced supercell lattice at provided temperature. The effect of the temperature is factored in as a thermal expansion as well as in the displacement of the generated supercells. 300 random configurations are found to be sufficient at lower temperatures (300 to 1000 K), while 500 configurations are needed at higher temperatures (1500 to 3500 K) to obtain converged force constants.

ShengBTE [44] is used to solve the BTE and calculate the 3ph and 4ph rates and κ_{ph}. The convergence of ShengBTE is tested and provided in the Supplemental Material [38]. Specifically, the 3ph calculation converges at a **q**-mesh density of 36×36×36, and the 3ph+4ph calculation converges at 12×12×12, respectively. Different extrinsic scattering rates, such as grain boundary scattering, defect scattering, and isotope scattering are calculated using their respective formulations. Phonon-electron scattering is calculated using density functional perturbation theory (DFPT) [47–49] and maximally localized Wannier functions using EPW [50–53]. Finally, total

scattering rates are obtained by adding all the phonon scattering rates and are used to calculate the intrinsic κ_{ph}.
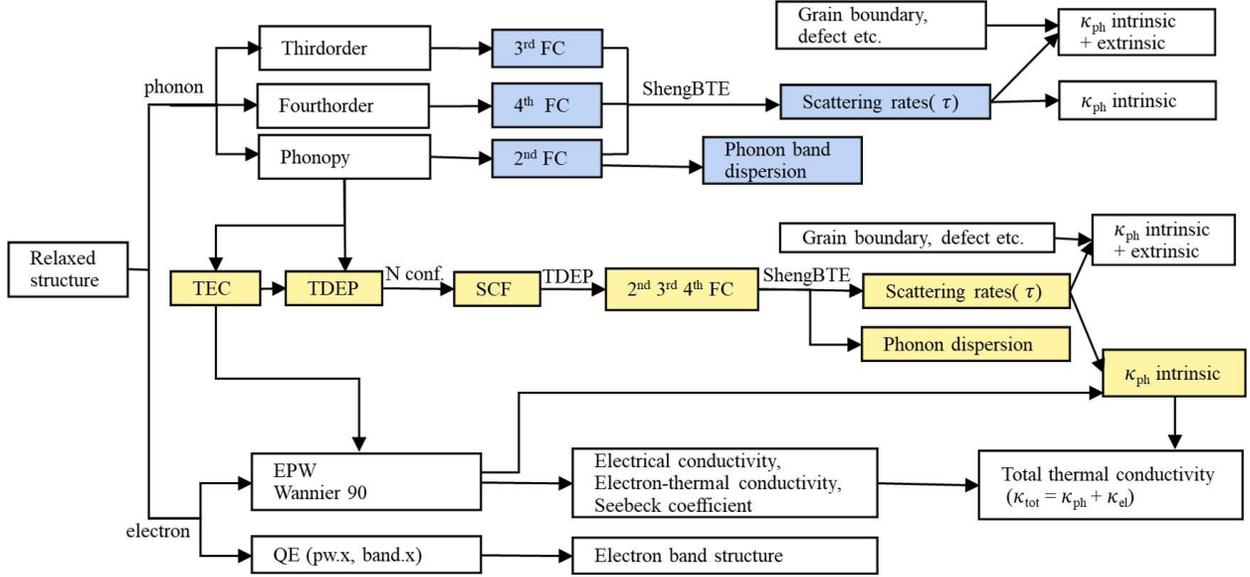
Figure 1: Computation workflow of this study.

Electronic contribution to κ is calculated using EPW [50–53] interfaced with Quantum Espresso [54,55]. The structure is relaxed with a **k**-mesh of $12 \times 12 \times 12$, a kinetic energy cutoff of 200 Ry, and Gaussian smearing with a spreading parameter of 0.002 Ry. Self-consistency is achieved using Davidson iterative diagonalization with a convergence threshold of 10^{-12}. Phonon-electron scattering rates are calculated using a $12 \times 12 \times 12$ **k**-mesh. Electron-phonon scattering rates are calculated using a coarse $6 \times 6 \times 6$ **q**-mesh and **k**-mesh and a fine $60 \times 60 \times 60$ **q**-mesh and **k**-mesh for convergence. The sp^3 and d entanglement is used for C and Zr, respectively. The electrons' velocities are calculated using the Wannier90 [56] under the EPW package. The Fermi window is selected so that the electron band dispersions obtained using the EPW package and DFT match with each other. Likewise, the outer window is selected so that it includes all the bands of interest. Finally, σ, $\kappa_{el,}$ and S are calculated.

III. RESULTS AND DISCUSSION

A. Thermal Expansion Coefficient
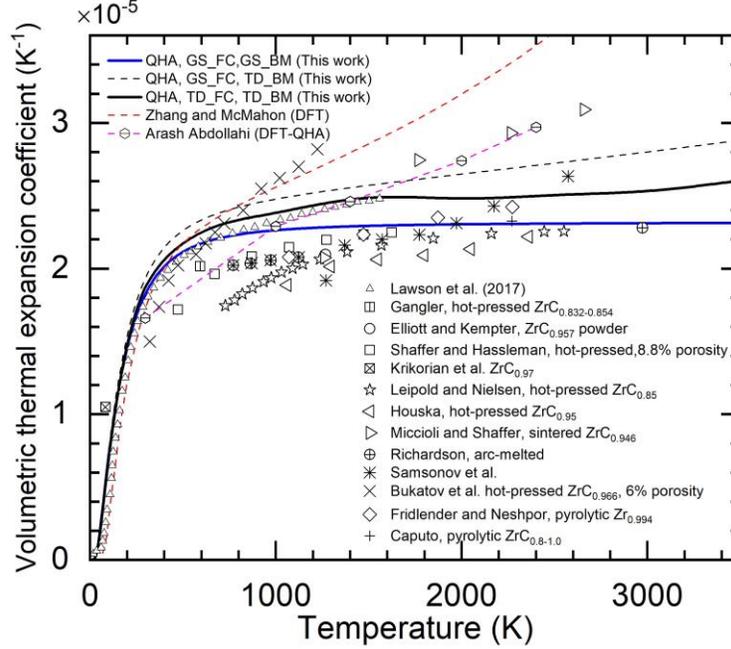
Figure 2: Predicted volumetric thermal expansion coefficient of ZrC as a function of temperature. The DFT predicted data by Zhang and McMahon [57] and Abdollahi [58], as well as different experimental data [4,23,56–58], are included for comparison.

The thermal expansion coefficient (TEC) is calculated using quasi-harmonic approximation (QHA) with the formalism found in Ref. [59]. As shown in Fig. 2, the predicted TEC (blue curve) deviates from experimental data at high temperatures, which is commonly seen for QHA. To resolve the discrepancy, we replace the constant bulk modulus (229 GPa [4]) in the formalism with temperature-dependent (TD) bulk modulus, and the predicted TEC (black dashed curve) agrees better with experimental data. After we include TDFC, the TEC (black solid curve) at high temperature agrees even better with experimental data. It is important to note that TD bulk modulus tends to increase the slope of TEC with temperature, while TDFC tends to decrease it. Overall, these findings suggest that utilizing TD bulk modulus and TDFC is a promising approach for the accurate prediction of TEC at high temperatures.

B. Temperature-dependent phonon band dispersion

The phonon dispersion relations of ZrC at 0, 300, 1000, and 3000 K are shown in Fig. 3, which match well with the experimental data [60–62]. The temperature softening effect in ZrC is not significant. The phonon dispersion calculated from TDEP at finite temperature deviates slightly from the ground state calculations. The partial density of states (PDOS) shows that the heavier metal Zr dominates the acoustic phonon of frequency (0-10 THz), while the lighter element C dominates the optical phonon of frequency (12-20 THz). Since the acoustic phonon modes contribute the most to lattice heat transfer, we can expect Zr vibration dominates the heat transfer.
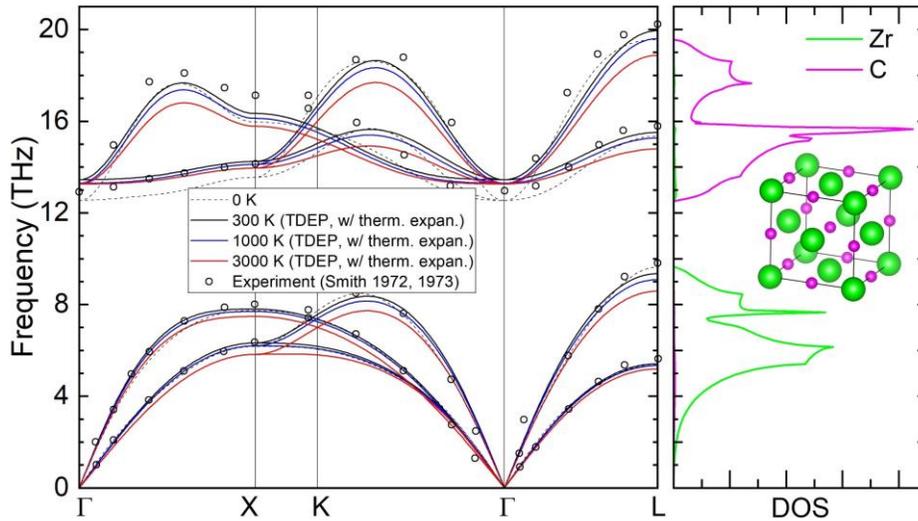
Figure 3: Phonon dispersion relations of ZrC at 0, 300,1000, and 3000 K, compared to the experimental data [60–62]. The right side shows the partial density of states of Zr and C at 0 K.

C. Scattering rates

The 3ph, 4ph, and ph-el rates, at three different temperatures of 300, 1000, and 3000 K are presented in Fig. 4. 3ph dominates throughout all temperatures, and 4ph becomes important at high temperatures, while ph-el is insignificant at all temperatures (even though a very small portion of phonons show high ph-el rates). 4ph plays a more important role in optical phonons than acoustic phonons, similar to the findings in Si, BAs, and diamond [30]. The large 4ph rates are due to the large acoustic-optical phonon band gap, which restricts 3ph processes.
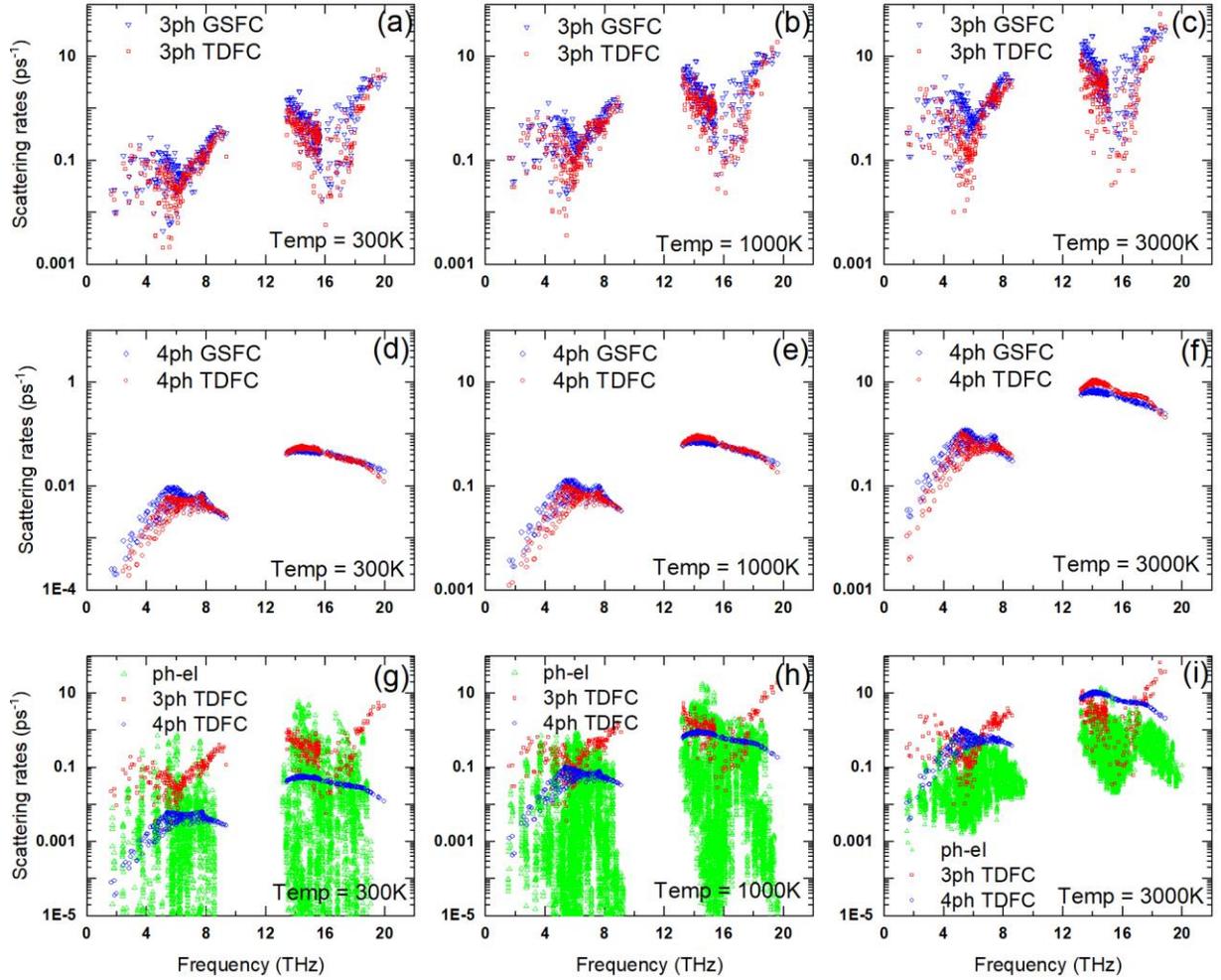
Figure 4: Comparison of 3ph (a, b, c), 4ph (d, e, f), and ph-el (g, h, i) scattering rates of ZrC at different temperatures. Results by using GSFC and TDFC are compared. GSFC indicates all 2FC, 3FC, and 4FC are ground-state. TDFC indicates all 2FC, 3FC, and 4FC are temperature-dependent.

Figures 4 (a-c) show the impacts of TDFC on 3ph rates at various temperatures. It is seen that TDFC decreases the 3ph rates at all temperatures. One reason is that the TD 2FC changes the phonon dispersion and reduces the 3ph phase space by making the 3ph processes' energy and momentum conservation rules harder to be satisfied, which has been widely discovered in many other materials [63,64]. We explicitly check the 3ph phase spaces of ZrC at 3000 K using GS and TD 2FC separately, as shown in Fig. 5 (a). It is seen that most modes are reduced even though some are increased. We have also compared the 3ph rates using GS and TD 2FC and found that

TD 2FC gives smaller 3ph rates than GS 2FC, as shown in Fig. 5 (e). The other reason is that the 3FC is softened by temperature [32]. As seen in Fig. 5 (f), using TD 3FC gives slightly smaller 3ph rates than using GS 3FC.
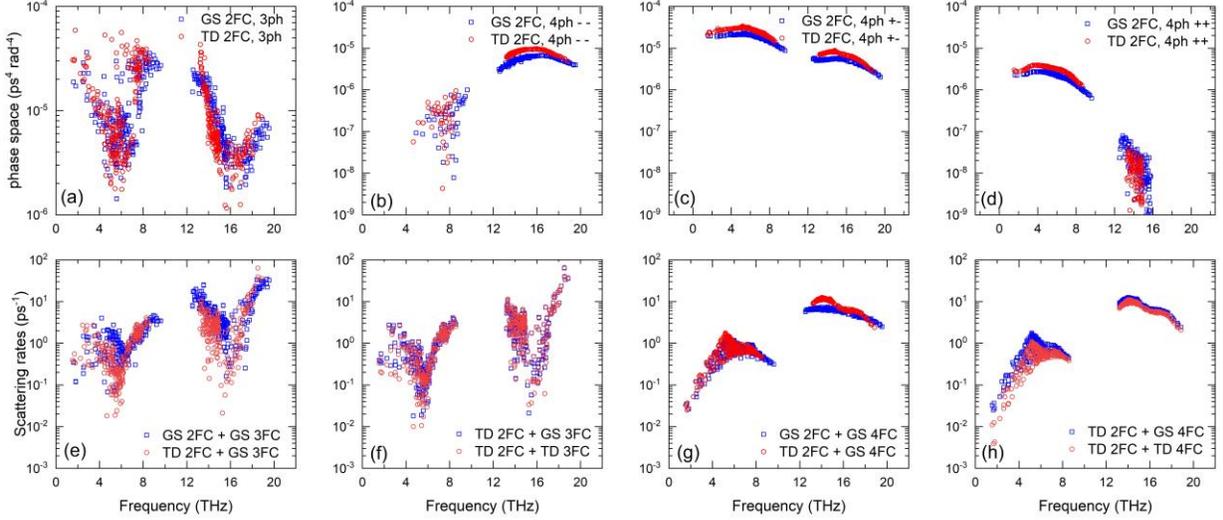
Figure 5: Effects of GS and TD FC on 3ph and 4ph phase space and rates at 3000 K. (a) Effect of TD 2FC on 3ph phase space. (b-d) Effect of TD 2FC on 4ph phase space. (b) is for splitting 4ph processes ($\lambda_1 \rightarrow \lambda_2 + \lambda_3 + \lambda_4$). (c) is for redistribution 4ph processes ($\lambda_1 + \lambda_2 \rightarrow \lambda_3 + \lambda_4$). (d) is for recombination 4ph processes ($\lambda_1 + \lambda_2 + \lambda_3 \rightarrow \lambda_4$). (e) Effect of TD 2FC on 3ph rates. (f) Effect of TD 3FC on 3ph rates. (g) Effect of TD 2FC on 4ph rates. (h) Effect of TD 4FC on 4ph rates.

Figures 4 (d-f) show the impacts of TDFC on 4ph rates at various temperatures. Interestingly, acoustic 4ph rates decrease while the optical 4ph rates increase when using the TDFC instead of the GSFC. This trend becomes more prominent as the temperature increases. To understand the physical reason behind this phenomenon and tell whether this is induced by the temperature dependence of 2FC or 4FC, we have done the following two comparisons at 3000 K. First, we compare the "GS 2FC + TD 4FC" and "TD 2FC + TD 4FC" to isolate the impact of TD 2FC. As shown in Fig. 5 (g), TD 2FC results in higher 4ph rates for both acoustic and optical phonons than GS 2FC. This is because TD 2FC flattens both acoustic and optical phonon dispersions, which makes the 4ph energy conservation rule easier to be satisfied, especially for the 4ph redistribution processes ($\lambda_1 + \lambda_2 \rightarrow \lambda_3 + \lambda_4$) where the modes λ_1 and λ_3 sit on the same flat band while the modes λ_2 and λ_4 sit on the other same flat band. This effect is clearly shown in Figs. 5 (b-d), which

shows the scattering phase space for splitting 4ph processes ($\lambda_1 \rightarrow \lambda_2 + \lambda_3 + \lambda_4$), labeled as "--",
redistribution 4ph processes ($\lambda_1 + \lambda_2 \rightarrow \lambda_3 + \lambda_4$), labeled as "+-", and recombination 4ph
processes ($\lambda_1 + \lambda_2 + \lambda_3 \rightarrow \lambda_4$), labeled as "++", respectively. It is seen that TD 2FC significantly
increases the scattering phase space. This effect is stronger for optical phonons than acoustic
phonons as optical branches are flattened more. Second, we compare the "TD 2FC + GS 4FC" and
"TD 2FC + TD 4FC" calculations to isolate the impact of TD 4FC. As seen in Fig. 5 (h), using TD
4FC gives smaller 4ph rates for both acoustic and optical phonons. This agrees with the fact that
TD 4FC reduces the scattering cross section, as found for UO_2 [32]. In summary, TD 2FC and TD
4FC have competing impacts, with the former increasing 4ph rates while the latter decreases them.
The impact of TD 2FC dominates for optical phonons while the impact of TD 4FC dominates for
acoustic phonons, which results in an increase of 4ph rates in optical phonon modes and a decrease
in acoustic phonon modes.

D. Phonon thermal conductivity calculation

Figure 6 shows the κ_{ph} as a function of temperature, using various force constants. In the following,
we track the changes of κ_{ph} at a low (300 K) and a high temperature (3500 K) when we gradually
increase the calculation comprehensivity. First, we calculate the basic 3ph thermal conductivity
using GSFC, which gives 56.9 and 6.3 W m^{-1} K^{-1} at 300 and 3500 K, respectively. When we replace
the GS 2FC with TD 2FC, κ_{ph} increases by 9% and 33% to 62.1 and 8.4 W m^{-1} K^{-1}, respectively.
Then, we include 4ph, and κ_{ph} decreases significantly by 2% and 75% to 61 and 2.1 W m^{-1} K^{-1},
respectively. After that, we replace the GS AFC with the TD AFC, and κ_{ph} increases by 0% and
52% to 61 and 3.2 W m^{-1} K^{-1}, respectively. This increase in κ_{ph} is attributed to the decrease in
scattering cross-section with increasing temperature [32]. In the end, we add the ph-el scattering,
and κ_{ph} slightly decreases by 10% to 55.0 and 2.9 W m^{-1} K^{-1} at 300 and 3500 K, respectively. The
inset illustrates the reduction of thermal conductivity by 4ph as a function of temperature. Further
analysis on 4ph using different force constants is provided in the Supplemental Material [38]. The
off-diagonal term, calculated from Wigner formalism, is not found to make a significant
contribution, unlike in some other materials [65,66]. Although the Wigner contribution increases
with temperature, it only reaches a maximum value of 0.2 W m^{-1} K^{-1} at 3500 K, which is much
lower than the standard Peierl κ_{ph} of 2.9 W m^{-1} K^{-1} at that temperature. Considering all these
intrinsic effects, the κ_{ph} is found to follow a temperature dependence of $\sim T^{-1.5}$ rather than $\sim T^{-1}$.
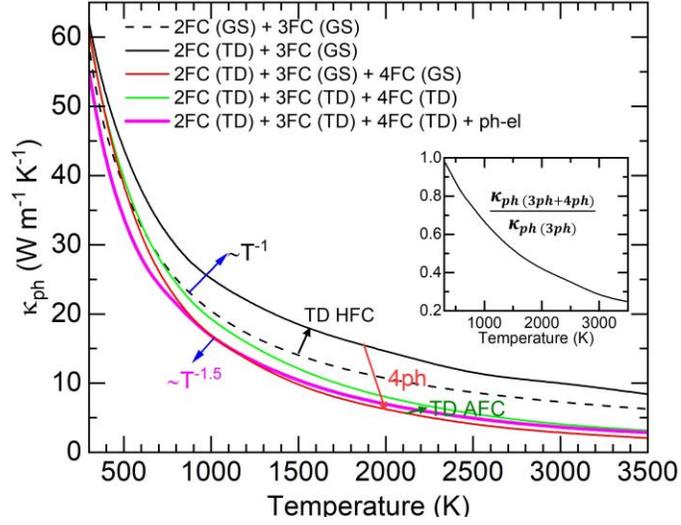
Figure 6: Temperature-dependent phonon thermal conductivity of ZrC calculated using different scattering mechanisms. The inset shows the relative contribution of 4ph rates compared to 3ph rates.

E. Electronic thermal conductivity calculation

The predicted electrical conductivity (σ) as a function of temperature is shown in Fig. 7. The experimental data along with the DFT prediction from Ref. [29] are also shown for comparison. The σ decreases with temperature monotonically as a result of the increase of electron-phonon scattering [34,67–69]. The σ calculated in this study is consistent with the results of stoichiometric ZrC obtained in Ref. [26] using ab initio molecular dynamics simulations. However, it should be noted that our σ prediction is higher than most of the experimental data, particularly at low temperatures. This could be because the DFT calculations assume a perfect crystal and do not consider the effects of defects (especially the carbon vacancies) and porosity that are present in experimental samples. This idea is supported by the findings in Ref. [26], where an increase in electrical resistivity (equivalently decrease in σ) is observed with impurities and defects in the sample. Furthermore, the Lorenz number (L) using the Wiedemann-Franz law: $L = \kappa_{el} / \sigma T$ is calculated, which is found to deviate significantly from the Sommerfeld value of 2.44×10^{-8} W Ω K^{-2} and vary from 1.6 to 3.3×10^{-8} W Ω K^{-2} at different temperatures. This deviation from the standard value highlights the limitations of using the Lorenz number to calculate κ_{el} from σ, as such an approach can lead to overprediction at lower temperatures and underprediction at higher temperatures.

12
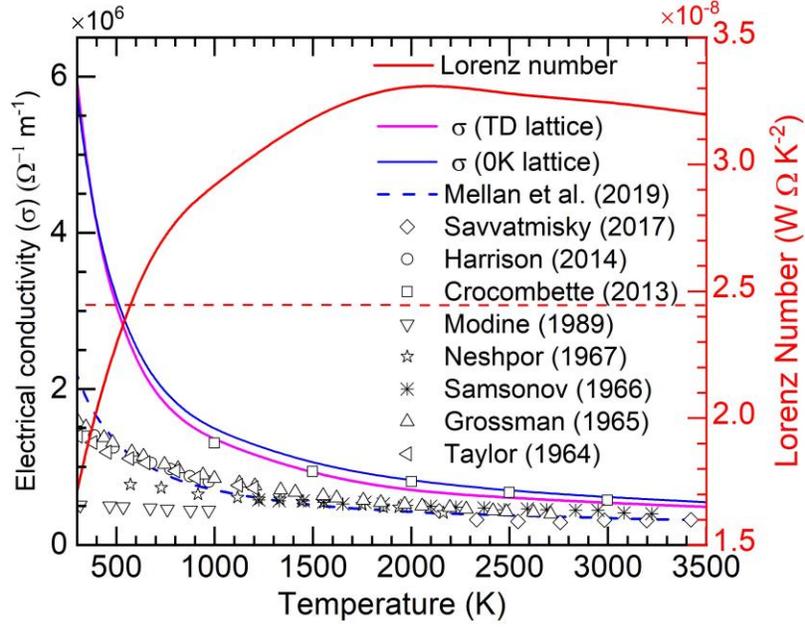
Figure 7: Electrical conductivity and Lorenz number of ZrC as a function of temperature. Literature data of electrical conductivity [2,4,5,21,22,26,29,70,71] are included for comparison.

The κ_{el} is compared to κ_{ph} as a function of temperature in Fig. 8. Phonons dominate thermal transport at lower temperatures whereas electrons dominate at higher temperatures, similar to results found in Refs. [26,29]. As temperature increases, e.g., from 300 K to 3500 K, κ_{el} increases from 30 W m^{-1} K^{-1} to 54.7 W m^{-1} K^{-1}, whereas κ_{ph} decreases from 55.0 W m^{-1} K^{-1} to 2.9 W m^{-1} K^{-1}. At room temperature, κ_{ph} accounts for roughly 70% of κ, which declines to just about 35% and 10% at 1000 and 3500 K respectively.
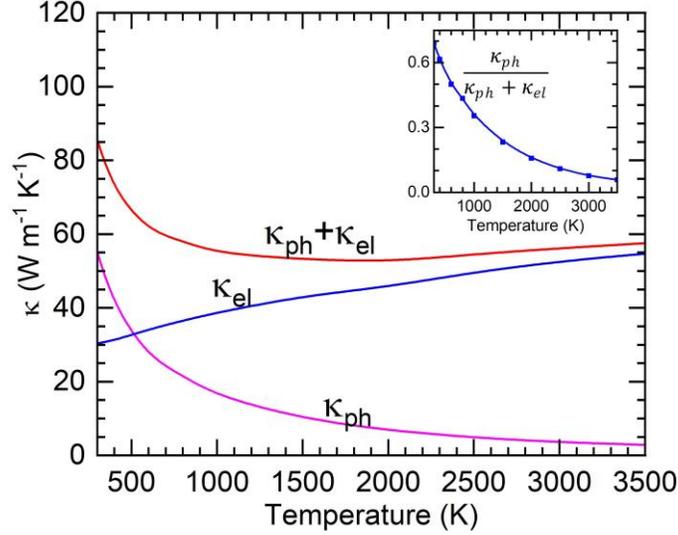
Figure 8: Temperature-dependent κ_{ph}, κ_{el}, and κ of ZrC. The inset shows the relative contribution of κ_{ph}.

In Fig. 9, the predicted κ (= κ_{ph} + κ_{el}) is compared to various experimental data. The blue-shaded and yellow-shaded region represents the contribution of κ_{el} and κ_{ph}, respectively. We can find that the experimental data are scattered and considerably lower than our prediction. This should be due to the presence of various defects, porosity, and vacancies in the experimental samples, which significantly decrease κ. Carbon vacancy is known to inevitably present in ZrC due to the intrinsic thermodynamic instability [72,73]. This decrease is much more significant at lower temperatures compared to higher temperatures due to the suppression of κ_{ph}. κ_{el} also gets suppressed due to impurities, defects, and vacancy scattering; however, the effect is smaller as found by Crocombette [26] through molecular dynamics. In that study, the predicted κ for stoichiometric ZrC was much higher than the reported experimental data. However, when some vacancy was introduced, both κ_{el}, and κ_{ph} decreased, and the predicted κ matched the experimental data. It is worth noting that our κ, as well as κ_{el}, matches Crocombette's [26] results with good accuracy.

We also compare our results to those predicted in Ref. [29] by first principles. We find that they underpredict κ_{el} and overpredict κ_{ph}. As a result, their total κ prediction agrees with ours at low and ultra-high temperatures, but is lower than ours in the intermediate temperature range, from 500 to 3000 K. In Ref. [29], at the temperature of 1500 K, κ_{ph} is overestimated by ~27.5% (9.93$\rightarrow$~12.67 W m^{-1} K^{-1}), and κ_{el} is underestimated by ~38% (43.21 $\rightarrow$ ~26.78 W m^{-1} K^{-1}), leading to κ underestimation of ~25.81% (53.15 $\rightarrow$ ~39.43 W m^{-1} K^{-1}). At ultra-high temperatures of 3500

14

K, κ_{ph} is overestimated by ~75% and κ_{el} is underestimated by ~8%, leading to a slight κ underestimation of ~4%. At lower temperatures of 300 K, κ_{ph} is overestimated by ~26.5% and κ_{el} is underestimated by ~50.6%, leading to a slight κ underestimation of ~1.0%. The matching of the predicted κ in Ref. [29] with experimental data is due to the error-cancellation effect where the prediction underpredicts the κ and the experimental samples' defects reduce κ.
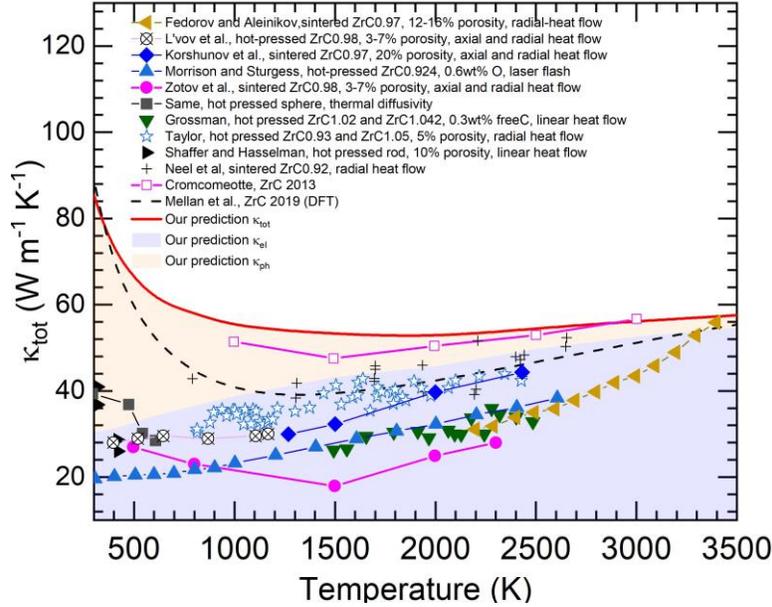
Figure 9: Comparison of our predicted thermal conductivity with various literature data collected by Jackson and Lee [4], and theoretical prediction by ab initio molecular dynamics [26] and DFT [29].

F. Effect of extrinsic defects and grain boundary

To understand the effect of extrinsic factors such as grain size, we calculate the cumulative thermal conductivity with respect to the mean free path (MFP). As shown in Fig. 10 (a), in bulk ZrC, 80% of κ_{ph} at 300, 1000, and 3000 K is contributed by the phonons with an MFP of less than 300, 60, and 20 nm, respectively. The effect of grain boundaries on thermal conductivity is more pronounced at lower temperatures. The MFP of electrons is much smaller than that of phonons. 80% of heat transfer occurs with electrons having MFPs less than 15, 4, and 0.7 nm. This suggests that the contribution of grain boundary scattering is much less significant for electrons compared to phonons. Figure 10 (b) shows the normalized κ_{ph} as a function of grain size from 10 to 10000 nm. The solid line represents the current method (TDFC, 3ph+4ph), while the dashed line represents the traditional approach (GSFC, 3ph). The graph explains how much κ_{ph} gets suppressed

(in terms of %) at various grain sizes and temperatures. For instance, if the grain boundary size is 100 nm, the κ_{ph} at 300, 1000, 2000, and 3000 K is roughly 55%, 76%, 87%, and 94% of the bulk values, respectively. The inset shows the grain size required to reduce κ_{ph} to 80% of the bulk values. At 300 and 3500 K, such grain sizes are 445 and 25 nm, respectively. The difference in grain boundary scattering between TDFC and GSFC is not substantial. Since the grain size in the experimental samples [2,4] is in the order of µm (~2 to 20 µm), the grain boundary scattering might not be the primary reason behind κ_{ph} suppression.
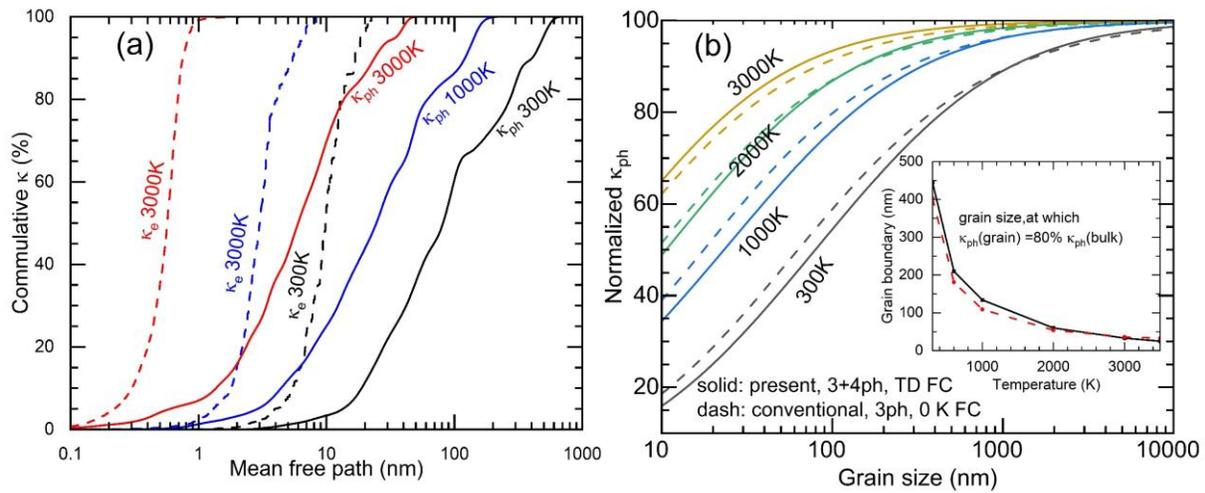
Figure 10: (a) Cumulative κ_{ph} and κ_{el} with mean free path at various temperatures. (b) Percentage normalized κ_{ph} as a function of grain size. The inset shows the grain size at which κ_{ph} is 80% of the bulk value.

The impact of carbon and zirconium vacancies on κ_{ph} of ZrC is calculated and found to be strong, using perturbation theory, as shown in Fig. 11 (a). For example, at 300 K, 1% and 2% carbon vacancies can decrease κ_{ph} by 39% and 56% respectively. The impact of Zr vacancy is even stronger, e.g., at 300 K, even 0.5% of Zr vacancy can lead to a decrease in κ_{ph} by 80%. This can be explained by the partial density of states presented in Fig. 3. Zr has a much larger mass than C and dominates the acoustic frequency bands, which dominate the heat transfer. A small concentration of Zr vacancy can lead to a significant decrease in κ_{ph}.

16

Figure 11 (b) displays κ of ZrC for various C/Zr ratios, with experimental data collected by Jackson and Lee [4] and DFT prediction by Mellan, Aziz, Xia, Grau-Crespo, and Duff [29]. The figure reveals that the experimental κ increases exponentially as the crystal structure approaches the stoichiometric ratio, which is in line with the trend predicted by DFT. It is worth noting that our prediction accounts only for the κ_{ph} suppression caused by C and Zr vacancies. If we include the κ_{ph} and κ_{el} suppression due to impurities, porosity, and grain boundaries as well, we can safely assume that our prediction will become lower and approaches the experimental value. This suggests that the experimental κ value does not reach the maximum theoretical limit of κ of ZrC, as κ_{ph} and κ_{el} are suppressed by the presence of vacancies, impurities, grain boundaries, and porosity in the sample.
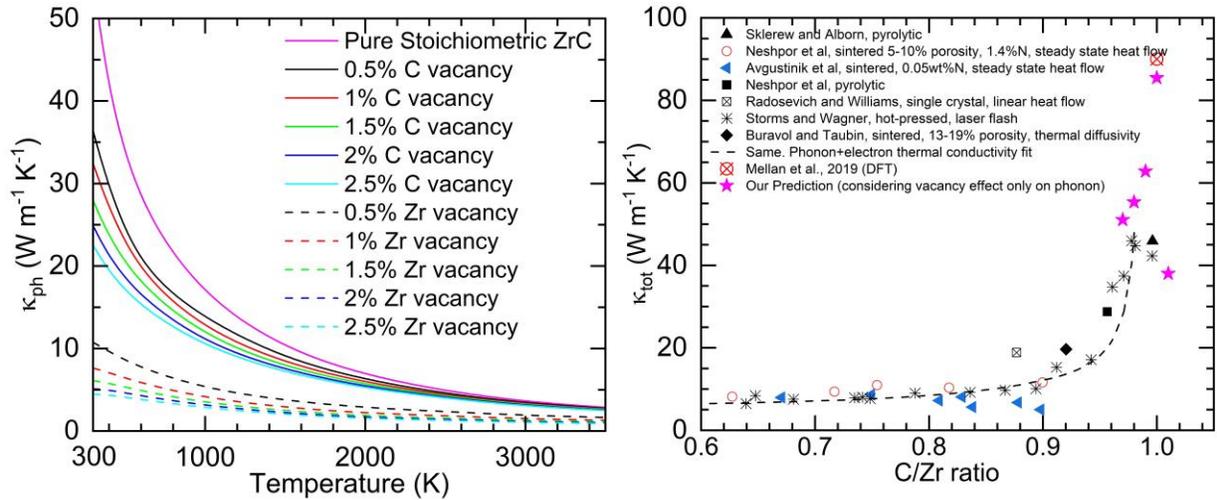
Figure 11: (a) Effect of C and Zr vacancy on phonon thermal conductivity of ZrC. (b)Variation of total thermal conductivity of ZrC with different C/Zr ratios. DFT prediction by Mellan *et al.* [29] and various experimental data collected by Jackson and Lee [4] are presented for comparison.

IV. CONCLUSIONS

In this study, the thermal transport of ZrC is predicted using the first principles calculations. Various factors affecting thermal transport, especially at high temperatures, are considered, including high-order phonon scattering, lattice expansion, TDFC, and inter-band phonon conduction. The following conclusions can be drawn. (1) TD bulk modulus and TDFC are important for the accurate prediction of TEC at high temperatures. (2) Phonons and electrons

dominate the heat transfer at lower and higher temperatures respectively. κ_{ph} contributes roughly 70% at room temperature and declines to about 35% and 10% when the temperature increases to 1000 and 3500 K, respectively. (3) The 4ph is important at high temperatures and reduces κ_{ph} by 2%, 34%, 59%, and 76% at 300, 1000, 2000, and 3500 K, respectively. (4) Although the electron-phonon scattering increases with temperature but its impact is much smaller than 3ph and 4ph scattering. (5) Interestingly, TD 2FC decreases 3ph rates but increases 4ph rates by decreasing and increasing the scattering phase spaces, respectively. For 4ph phase space, the TD 2FC flattens phonon bands, and allow more redistribution 4ph processes ($\lambda_1 + \lambda_2 \rightarrow \lambda_3 + \lambda_4$) to happen. (6) We confirm that the TD 3FC and 4FC decrease the phonon scattering cross-section at elevated temperatures and increase the κ_{ph} significantly in metals (by 52% at 3500 K), in addition to that found in insulators [32]. (7) The combination effect of TD 2FC and TD 4FC reduces 4ph rates of acoustic modes but increases those of optical modes. (8) The maximum Wigner off-diagonal (diffuson) contribution to κ_{ph} (0.2 W m^{-1} K^{-1}) is much lower compared to standard Peierls phonon contribution κ_{ph} (2.9 W m^{-1} K^{-1} at 3500 K). (9) The σ decreases monotonically while κ_{el} increases as temperature increases. The Lorenz number (L) deviates significantly from the Sommerfeld value of L_0 =2.44×10^{-8} W Ω K^{-2}, highlighting the limitations of using the L_0 to calculate κ_{el}. (10) No experimental data have reached the predicted intrinsic thermal conductivity values due to the presence of inherent defects in the experimental samples. The matching of κ predicted in the literature with experimental data is due to the error-cancellation effect where the prediction underpredicts the κ and the experimental samples' defects reduce κ. Overall, our study makes a critical revisit to the thermal transport from room to ultra-high temperatures.

Data availability

Source data are provided along with this paper. All other data that support the plots within this paper are available from the corresponding authors on reasonable request.

Code availability

The codes used in this study are available from the corresponding authors upon request.

Author contributions

T.F. conceived the idea and guided the project. J.T performed the simulations and wrote the original manuscript. J.T and T.F. both revised the manuscript.

Competing interests

The authors declare no competing interests.

Additional information

Correspondence and requests for materials should be addressed to T.F.

REFERENCES:

[1] A. Fernández Guillermet, *Analysis of Thermochemical Properties and Phase Stability in the Zirconium-Carbon System*, J. Alloys Compd. **217**, 69 (1995).

[2] A. I. Savvatimskiy, S. V. Onufriev, and S. A. Muboyadzhyan, *Measurement of ZrC Properties up to 5000 K by Fast Electrical Pulse Heating Method*, J. Mater. Res. **32**, 1287 (2017).

[3] C. C. Sorrell, V. S. Stubican, and R. C. Bradt, *Mechanical Properties of ZrC- ZrB2 and ZrC- TiB2 Directionally Solidified Eutectics*, J. Am. Ceram. Soc. **69**, 317 (1986).

[4] H. F. Jackson and W. E. Lee, *Properties and Characteristics of Zrc*, Vol. 2 (Elsevier Inc., 2012).

[5] R. W. W. Harrison and W. E. E. Lee, *Processing and Properties of ZrC, ZrN and ZrCN Ceramics: A Review*, Adv. Appl. Ceram. **115**, 294 (2016).

[6] D. Cheng, S. Wang, and H. Ye, *First-Principles Calculations of the Elastic Properties of*

ZrC and ZrN, J. Alloys Compd. **377**, 221 (2004).

[7]   D. Sciti, S. Guicciardi, and M. Nygren, *Spark Plasma Sintering and Mechanical Behaviour of ZrC-Based Composites*, Scr. Mater. **59**, 638 (2008).

[8]   K. Upadhya, J.-M. Yang, and W. P. Hoffman, *Materials for Ultrahigh Temperature Structural Applications*, Am. Ceram. Soc. Bull. **76**, 51 (1997).

[9]   G. M. Song, Y. J. Wang, and Y. Zhou, *Elevated Temperature Ablation Resistance and Thermophysical Properties of Tungsten Matrix Composites Reinforced with ZrC Particles*, J. Mater. Sci. **36**, 4625 (2001).

[10]   Q. Tong, J. Shi, Y. Song, Q. Guo, and L. Liu, *Resistance to Ablation of Pitch-Derived ZrC/C Composites*, Carbon N. Y. **42**, 2495 (2004).

[11]   M. B. Dickerson, P. J. Wurm, J. R. Schorr, W. P. Huffman, P. G. Wapner, and K. H. Sandhage, *Near Net-Shape, Ultra-High Melting, Recession-Resistant ZrC/W-Based Rocket Nozzle Liners via the Displacive Compensation of Porosity (DCP) Method*, J. Mater. Sci. **39**, 6005 (2004).

[12]   Y. Xu, W. Sun, X. Xiong, F. Liu, and X. Luan, *Ablation Characteristics of Mosaic Structure ZrC-SiC Coatings on Low-Density, Porous C/C Composites*, J. Mater. Sci. Technol. **35**, 2785 (2019).

[13]   A. Paul, S. Venugopal, J. Binner, B. Vaidhyanathan, D. D. Jayaseelan, E. Zapata-Solvas, W. E. Lee, A. Heaton, and P. Brown, *UHTC Composites for Hypersonic Applications*, Am. Ceram. Soc. Bull. **91**, 22 (2012).

[14]   Y. Katoh, G. Vasudevamurthy, T. Nozawa, and L. L. L. L. Snead, *Properties of Zirconium Carbide for Nuclear Fuel Applications*, J. Nucl. Mater. **441**, 718 (2013).

[15]   L. L. Snead, Y. Katoh, and S. Kondo, *Effects of Fast Neutron Irradiation on Zirconium Carbide*, J. Nucl. Mater. **399**, 200 (2010).

[16]   K. Schönfeld, M. Trache, and H. P. Martin, *Electrical Performance of ZrC Ceramics*, Materwiss. Werksttech. **52**, 1338 (2021).

[17]   A. V. Kostanovskiy, M. E. Kostanovskaya, M. G. Zeodinov, and A. A. Pronkin, *Electrical Resistivity of Zirconium Carbide at 1200-2500 K*, J. Phys. Conf. Ser. **1787**, (2021).

[18]   R. E. Taylor, *Thermal Conductivity of Zirconium Carbide at High Temperatures*, J. Am. Ceram. Soc. **45**, 353 (1962).

[19]   B. Wei, L. Chen, Y. Wang, H. Zhang, S. Peng, J. Ouyang, D. Wang, and Y. Zhou,

Densification, Mechanical and Thermal Properties of ZrC1 − x Ceramics Fabricated by Two-Step Reactive Hot Pressing of ZrC and ZrH2 Powders, J. Eur. Ceram. Soc. **38**, 411 (2018).

[20] X. Wei, C. Back, O. Izhvanov, C. D. Haines, and E. A. Olevsky, *Zirconium Carbide Produced by Spark Plasma Sintering and Hot Pressing: Densification Kinetics, Grain Growth, and Thermal Properties*, Materials (Basel). **9**, (2016).

[21] R. E. Taylor and J. Morreale, *Thermal Conductivity of Titanium Carbide, Zirconium Carbide, and Titanium Nitride at High Temperatures*, J. Am. Ceram. Soc. **47**, 69 (1964).

[22] L. N. Grossman, *High‐ Temperature Thermophysical Properties of Zirconium Carbide*, J. Am. Ceram. Soc. **48**, 236 (1965).

[23] M. H. Leipold and T. H. Nielson, Mechanical Properties of Hot- Pressed Zirconium Carbide Tested to 2600°C, 1964.

[24] R. E. B. Makinson, *The Thermal Conductivity of Metals*, Math. Proc. Cambridge Philos. Soc. **34**, 474 (1938).

[25] E. Grüneisen and H. Reddemann, *Elektronen‐ Und Gitterleitung Beim Wärmefluß in Metallen*, Ann. Phys. **412**, 843 (1934).

[26] J. P. Crocombette, *Origins of the High Temperature Increase of the Thermal Conductivity of Transition Metal Carbides from Atomistic Simulations*, J. Phys. Condens. Matter **25**, (2013).

[27] Y. Zhou, W. G. Fahrenholtz, J. Graham, and G. E. Hilmas, *From Thermal Conductive to Thermal Insulating: Effect of Carbon Vacancy Content on Lattice Thermal Conductivity of ZrCx*, J. Mater. Sci. Technol. **82**, 105 (2021).

[28] Y. Zhou, W. G. Fahrenholtz, J. Graham, and G. E. Hilmas, *Electronic Structure and Thermal Conductivity of Zirconium Carbide with Hafnium Additions*, J. Am. Ceram. Soc. **104**, 4708 (2021).

[29] T. A. Mellan, A. Aziz, Y. Xia, R. Grau-Crespo, and A. I. Duff, *Electron and Phonon Interactions and Transport in the Ultrahigh-Temperature Ceramic ZrC*, Phys. Rev. B **99**, 1 (2019).

[30] T. Feng, L. Lindsay, and X. Ruan, *Four-Phonon Scattering Significantly Reduces Intrinsic Thermal Conductivity of Solids*, Phys. Rev. B **96**, 161201 (2017).

[31] X. Yang, T. Feng, J. Li, and X. Ruan, *Stronger Role of Four-Phonon Scattering than Three-*

Phonon Scattering in Thermal Conductivity of III-V Semiconductors at Room Temperature, Phys. Rev. B **100**, 245203 (2019).

[32]   X. Yang, J. Tiwari, and T. Feng, *Reduced Anharmonic Phonon Scattering Cross-Section Slows the Decrease of Thermal Conductivity with Temperature*, Mater. Today Phys. **24**, 100689 (2022).

[33]   G. D. Mahan, *Many-Particle Physics* (Springer Science & Business Media, 2000).

[34]   Z. Tong, S. Li, X. Ruan, and H. Bao, *Comprehensive First-Principles Analysis of Phonon Thermal Conductivity and Electron-Phonon Coupling in Different Metals*, Phys. Rev. B **100**, 144306 (2019).

[35]   C. A. Ratsifaritana and P. G. Klemens, *Scattering of Phonons by Vacancies*, Int. J. Thermophys. **8**, 737 (1987).

[36]   G. Xie, Y. Shen, X. Wei, L. Yang, H. Xiao, J. Zhong, and G. Zhang, *A Bond-Order Theory on the Phonon Scattering by Vacancies in Two-Dimensional Materials*, Sci. Rep. **4**, 5085 (2014).

[37]   B. Xu, T. Feng, Z. Li, S. T. Pantelides, and Y. Wu, *Constructing Highly Porous Thermoelectric Monoliths with High-Performance and Improved Portability from Solution-Synthesized Shape-Controlled Nanocrystals*, Nano Lett. **18**, 4034 (2018).

[38]   *See Supplemental Materials at [Link] for Additional Information*, (n.d.).

[39]   G. Kresse and J. Hafner, *Ab Initio Molecular Dynamics for Liquid Metals*, Phys. Rev. B **47**, 558 (1993).

[40]   G. Kresse and J. Furthmüller, *Efficiency of Ab-Initio Total Energy Calculations for Metals and Semiconductors Using a Plane-Wave Basis Set*, Comput. Mater. Sci. **6**, 15 (1996).

[41]   G. Kresse, *From Ultrasoft Pseudopotentials to the Projector Augmented-Wave Method*, Phys. Rev. B - Condens. Matter Mater. Phys. **59**, 1758 (1999).

[42]   J. P. Perdew, K. Burke, and M. Ernzerhof, *Generalized Gradient Approximation Made Simple*, Phys. Rev. Lett. **77**, 3865 (1996).

[43]   A. Togo and I. Tanaka, *First Principles Phonon Calculations in Materials Science*, Scr. Mater. **108**, 1 (2015).

[44]   W. W. Li, J. Carrete, N. A. N. A. Katcho, and N. Mingo, *ShengBTE: A Solver of the Boltzmann Transport Equation for Phonons*, Comput. Phys. Commun. **185**, 1747 (2014).

[45]   O. Hellman, I. A. Abrikosov, and S. I. Simak, *Lattice Dynamics of Anharmonic Solids from*

First Principles, Phys. Rev. B - Condens. Matter Mater. Phys. **84**, 2 (2011).

[46]   O. Hellman, P. Steneteg, I. A. Abrikosov, and S. I. Simak, *Temperature Dependent Effective Potential Method for Accurate Free Energy Calculations of Solids*, Phys. Rev. B - Condens. Matter Mater. Phys. **87**, 104111 (2013).

[47]   S. Baroni, P. Giannozzi, and A. Testa, *Greens-Function Approach to Linear Response in Solids*, Phys. Rev. Lett. **58**, 1861 (1987).

[48]   S. Baroni, S. De Gironcoli, A. Dal Corso, and P. Giannozzi, *Phonons and Related Crystal Properties from Density-Functional Perturbation Theory*, Rev. Mod. Phys. **73**, 515 (2001).

[49]   X. Gonze and C. Lee, *Dynamical Matrices, Born Effective Charges, Dielectric Permittivity Tensors, and Interatomic Force Constants from Density-Functional Perturbation Theory*, Phys. Rev. B - Condens. Matter Mater. Phys. **55**, 10355 (1997).

[50]   S. Poncï et al., *EPW: Electron–Phonon Coupling, Transport and Superconducting Properties Using Maximally Localized Wannier Functions*, Comput. Phys. Commun. **209**, 116 (2016).

[51]   F. Giustino, M. L. Cohen, and S. G. Louie, *Electron-Phonon Interaction Using Wannier Functions*, Phys. Rev. B - Condens. Matter Mater. Phys. **76**, 1 (2007).

[52]   E. R. Margine and F. Giustino, *Anisotropic Migdal-Eliashberg Theory Using Wannier Functions*, Phys. Rev. B - Condens. Matter Mater. Phys. **87**, 1 (2013).

[53]   J. Noffsinger, F. Giustino, B. D. B. D. Malone, C. H. C.-H. Park, S. G. S. G. Louie, and M. L. M. L. Cohen, *EPW: A Program for Calculating the Electron-Phonon Coupling Using Maximally Localized Wannier Functions*, Comput. Phys. Commun. **181**, 2140 (2010).

[54]   P. Giannozzi et al., *QUANTUM ESPRESSO: A Modular and Open-Source Software Project for Quantum Simulations of Materials*, J. Phys. Condens. Matter **21**, (2009).

[55]   P. Giannozzi et al., *Advanced Capabilities for Materials Modelling with Quantum ESPRESSO*, J. Phys. Condens. Matter **29**, (2017).

[56]   A. A. Mostofi, J. R. J. R. Yates, G. Pizzi, Y. S. Y.-S. Lee, I. Souza, D. Vanderbilt, and N. Marzari, *An Updated Version of Wannier90: A Tool for Obtaining Maximally-Localised Wannier Functions*, Comput. Phys. Commun. **185**, 2309 (2014).

[57]   J. Zhang and J. M. McMahon, *Temperature-Dependent Mechanical Properties of ZrC and HfC from First Principles*, J. Mater. Sci. **56**, 4266 (2021).

[58]   A. Abdollahi, *First-Principle Calculations of Thermodynamic Properties of ZrC and ZrN*

at High Pressures and High Temperatures, Phys. B Condens. Matter **410**, 57 (2013).

[59] T. Feng, X. Yang, and X. Ruan, *Phonon Anharmonic Frequency Shift Induced by Four-Phonon Scattering Calculated from First Principles*, J. Appl. Phys. **124**, (2018).

[60] H. G. Smith, N. Wakabayashi, and M. Mostoller, *Superconductivity in D-and f-Band Metals*, in *AIP Conference Proceedings* (1972), p. 293.

[61] P. T. Jochym and K. Parlinski, *Ab Initio Lattice Dynamics and Elastic Constants of ZrC*, Eur. Phys. J. B **15**, 265 (2000).

[62] H. G. Smith and W. Gläser, *Phonon Spectra in TaC and HfC*, Phys. Rev. Lett. **25**, 1611 (1970).

[63] Y. Xia, *Revisiting Lattice Thermal Transport in PbTe: The Crucial Role of Quartic Anharmonicity*, Appl. Phys. Lett. **113**, 073901 (2018).

[64] Y. Xia, V. I. Hegde, K. Pal, X. Hua, D. Gaines, S. Patel, J. He, M. Aykol, and C. Wolverton, *High-Throughput Study of Lattice Thermal Conductivity in Binary Rocksalt and Zinc Blende Compounds Including Higher-Order Anharmonicity*, Phys. Rev. X **10**, (2020).

[65] M. Simoncelli, N. Marzari, and F. Mauri, *Wigner Formulation of Thermal Transport in Solids*, Phys. Rev. X **12**, 41011 (2022).

[66] M. Simoncelli, N. Marzari, and F. Mauri, *Unified Theory of Thermal Transport in Crystals and Glasses*, Nat. Phys. **15**, 809 (2019).

[67] S. Li, Z. Tong, X. Zhang, and H. Bao, *Thermal Conductivity and Lorenz Ratio of Metals at Intermediate Temperatures with Mode-Level First-Principles Analysis*, Phys. Rev. B **102**, 174306 (2020).

[68] X. Gu, S. Li, and H. Bao, Thermal Conductivity of Intrinsic Semiconductor at Elevated Temperature: Role of Four-Phonon Scattering and Electronic Heat Conduction, n.d.

[69] X. Gu, S. Li, and H. Bao, *Thermal Conductivity of Silicon at Elevated Temperature: Role of Four-Phonon Scattering and Electronic Heat Conduction*, Int. J. Heat Mass Transf. **160**, 120165 (2020).

[70] R. Harrison, O. Ridd, D. D. Jayaseelan, and W. E. Lee, *Thermophysical Characterisation of ZrCx Ny Ceramics Fabricated via Carbothermic Reduction-Nitridation*, J. Nucl. Mater. **454**, 46 (2014).

[71] F. A. Modine, M. D. Foegelle, C. B. Finch, and C. Y. Allison, *Electrical Properties of Transition-Metal Carbides of Group IV*, Phys. Rev. B **40**, 9558 (1989).

[72] Y. Zhou, T. W. Heitmann, W. G. Fahrenholtz, and G. E. Hilmas, *Synthesis of ZrC x with Controlled Carbon Stoichiometry by Low Temperature Solid State Reaction*, J. Eur. Ceram. Soc. **39**, 2594 (2019).

[73] Y. Zhou, T. W. Heitmann, E. Bohannan, J. C. Schaeperkoetter, W. G. Fahrenholtz, and G. E. Hilmas, *Carbon Vacancy Ordering in Zirconium Carbide Powder*, J. Am. Ceram. Soc. **103**, 2891 (2020).